Electronic Supplementary Material (ESI) for Materials Horizons.
This journal is © The Royal Society of Chemistry 2020

Supplementary Materials for

Bone-Inspired Healing of 3D-Printed Porous Ceramics

An Xin[1], Kunhao Yu[1], Runrun Zhang[1], Bingyuan Ruan[1], Allyson L. McGaughey[1], Zhangzhengrong Feng[1], Kyung Hoon Lee[1], Yong Chen[2], Amy E. Childress[1], Qiming Wang[1*]

[1]Sonny Astani Department of Civil and Environmental Engineering, University of Southern California, Los Angeles, CA 90089, USA

[2]Epstein Department of Industrial and Systems Engineering, University of Southern California, Los Angeles, CA 90089

*Email: qimingw@usc.edu

1. Materials and Methods

Materials. Poly (methyl-silsesquioxane) (MK) was purchased from Gelest. Tetrahydrofuran (THF), tri (propylene glycol) methyl ether (DOWANOL), 3-(Trimethoxysilyl) propyl methacrylate (TMSPM), phenylbis (2,4,6-trimethylbenzoyl) phosphine oxide (photo initiator), Sudan I (photo absorber), and ethanol were purchased from Sigma-Aldrich. Polymethylmethacrylate (PMMA) powders (with mean particle sizes of 6, 48, 100, and 200 μm) were purchased from Goodfellow. Hydrochloric acid was purchased from GR ACS. *Sporosarcina pasteurii* (ATCC 11859, non-infectious) was purchased from ATCC. To prepare the BPU medium (ATCC 1832) and the precipitation medium, tryptone, ammonium sulfate, ammonium chloride, sodium bicarbonate, and calcium chloride were purchased from Sigma-Aldrich. Urea, tricine, yeast extract, agar, and L-glutamic acid were purchased from Alfa Aesar. Difco nutrient broth was purchased from Fisher Scientific. All chemicals were used without further purification.

Preparation of preceramic photopolymers. 10 g MK powders were first dissolved into a premixed solvent of 10 mL THF and 10 mL DOWANOL by stirring for 24 h. 18 g of 48 μm PMMA particles were added and mixed well with the solution by stirring for 2 h. Thereafter, 2.5 mL of TMSPM was added into the solution and hydrolyzed in an acidic condition with 1ml HCl and 2ml deionized water (1). After 45 min of stirring, 1.5 g PI and 0.03 g Sudan I were added into the resin and mixed well by stirring for another 20 min.

Manufacturing of polymer-derived ceramic structures. The additive manufacturing of the preceramic polymer structures was performed using a projection stereolithography system (**Fig. S1**) (2-4). A computer-aided-design (CAD) model was first sliced into sequential images that were projected to a liquid basin with the preceramic photopolymer ink. The exposed resin was solidified

by light exposure, forming a solid layer bonded onto the printing stage. As the printing stage was lifted, the fresh resin refluxed beneath the printing stage. By lowering the stage a prescribed height and illuminating the resin with another slice image, a second layer was printed and bonded onto the first layer. These processes were repeated; each layer was set as 80 μm thickness and required 26 s to solidify. The 3D-printed preceramic structure was then dried in air at room temperature for 24 h and subsequently pyrolyzed in a tube furnace (Thermo Scientific Lindberg/Bule M TF55030A). The furnace temperature was programmed to increase from 25 to 350°C over 3 h 30 min and then keep at 350 °C for 1 h in airflow (**Fig. S3**). Then, the furnace continued to heat up from 350 to 1000 °C over 10 h and then keep at 1000 °C over 1 h in a nitrogen atmosphere (99.998%). Finally, the furnace was cooled from 1000 to 25 °C over 4 h 30 min in a nitrogen atmosphere.

Medium for microorganism growth and crystal precipitation. BPU medium (ATCC 1832 medium) containing 10 g/L tryptone, 5 g/L yeast extract, 4.5 g/L tricine, 5 g/L ammonium sulfate, 2 g/L glutamic acid, and 10 g/L urea was adjusted to PH 8.6±0.1 using a NaOH solution, and then filter-sterilized with a 0.2-μm autoclaved filter. To prepare the precipitation medium, 3 g Difco nutrient broth, 20 g urea, 10 g ammonium chloride, and 2.12 g sodium bicarbonate were dissolved into 1 L deionized water. After adjusting the pH below 6.0, the solution was autoclaved at 121 °C and 21 psi for 45 min. Subsequently, 28 g $CaCl_2$ was added and mixed into the cooled solution. The precipitation experiments were performed at 25 °C (5, 6). Agar aqueous solution was autoclaved separately and added to obtain a solid medium. *Sporosarcina pasteurii* (ATCC 11859) was inoculated and grown in the solid medium for two days at 30 °C. Then the inoculated bacteria were transferred to the BPU medium to grow for one day at 30 °C. All glassware was autoclaved at 121 °C and 21 psi for 15 min before use.

Bacteria-assisted healing process. A porous ceramic sample (**Figs. 1-3**) was soaked in 150 ml BPU medium with bacteria for 24 h at 30 °C. The cell concentration in the growth medium is around 0.8×10^8 -1.4×10^8 cells/mL, which was determined by reading the optical density at 600 nm (Thermo Scientific NanoDrop UV-Vis Spectrophotometer). Then, a 3PB load was used to break the sample into two parts (**Fig. S8**). The fractured ceramic structures were fixed tightly with glass supports and VHB tapes leaving a ~300 μm-wide crack between the two broken parts (**Fig. S5**). After this, the fixed structures were immersed in 150 ml precipitation medium. The precipitation medium was changed every 24 h and kept in an incubator at 25 °C. For the porous ceramic samples in Fig. 4, a compression load was used to break the structure into two parts, and then the relative position of two broken parts was fixed as described above. Afterward, we dropped the BPU medium with bacteria around the fracture interface and added more every 2 h for over 24 h; moisture was controlled with wet cotton. Then, we immersed the fixed structure into the precipitation medium for interfacial precipitation.

Healing of ceramic bones. The ceramic bones were made by sintering 3D-printed preceramic polymer structures in a bone-shape. The interfacial microstructures, bacteria, and precipitations were imaged using an SEM (JEOL JSM-7001). Corrosion experiments were carried out by dropping NaOH solution (4.8 mol/L) and H_2O_2 solution (8.8 mol/L) onto the healed interface or rinsing the sample in these solutions. The fire used to test the healed sample was ignited from a mixture of ethanol (70%) and water (30%). The fire temperature was measured as 650-750 °C (Poster digital thermocouple thermometer, **Fig. S7**). Annealing of the healed sample was carried out in the tube furnace with a programmed temperature history (**Fig. S9**). The 3PB tests were carried out using an Instron mechanical tester (Model 5942) (**Fig. S8**). The span between the two supporting points was 9.5 mm. Healing experiments were repeated after rebreaking the healing

interface, washing with hydrochloric acid (38 wt. %) and then pure ethanol and DI water, and drying in air for 4 h.

Characterization of healing performance. Dimensions of the rectangular polymer plate were 8 mm × 24 mm × 2 mm. All samples were pyrolyzed, broken, and healed according to the aforementioned process. After a predetermined duration (2-14 days), ceramic pieces were taken out, washed with pure ethanol, and dried in air for 4 h. 3PB tests were carried out using the Instron mechanical tester. Flexural strength is calculated as $S = (3F_m L)/(2bh^2)$, where F_m is maximal load, L is span between two supporting points, b is sample width, and h is sample thickness (inset of **Fig. 2D**). The Young's moduli of the healed ceramic samples were measured using compression tests. The cyclic healing experiments were carried out by contacting the broken ceramic samples, fastening the relative distance to leave a ~300μm gap, and exposing the fracture interface to bacteria and precipitation medium.

Cohesive fracture simulation. The cohesive fracture simulations were carried out using ABAQUS 6.14. 2D plane-stress models with three parts (two ceramic elements and the center cohesive element) were constructed (**Fig. S15A**). Bilinear traction-separation laws were employed to model the cohesive zone elements (**Fig. S15B**). Quadratic stress criterion was used to determine the damage initiation, written as

$$\left(\frac{t_n}{t_n^0}\right)^2 + \left(\frac{t_s}{t_s^0}\right)^2 + \left(\frac{t_t}{t_t^0}\right)^2 = 1 \quad (1)$$

where t_n, t_s, and t_t are nominal stresses in the normal and shear directions, and t_n^0, t_s^0, and t_t^0 are the corresponding strengths. In the simulation, we set t_n^0 as the tensile strength of the cohesive element ($t_n^0 = t_s^0 = t_t^0$, parameters shown in **Table S2**). We employed CPS4R elements to model

the ceramic parts and COH2D4 elements to model the cohesive zone. Simulation accuracy was ensured through a mesh refinement study.

Healing of ceramic dental crowns. Ceramic dental crowns were made by sintering 3D-printed preceramic polymer structures in a crown shape. Compression loads on the crowns were applied using a transverse metal rod. Finite element simulations were carried out using ABAQUS 6.14. The material parameters of the ceramic part included Young's modulus of 175 MPa and Poisson's ratio of 0.3. The models are discretized by C3D8R elements.

Healing of water membranes. Ceramic water treatment membranes were made by sintering 3D-printed preceramic polymer structures in flat-sheet and tubular configurations. The filtration of wastewater and measurement of hydraulic permeability were carried out using a set-up shown in **Fig. S20**. The wastewater with unknown particle suspensions was obtained from the drain pipe of the lab. To measure permeability, we sealed the ceramic membrane using VHB tape and fixed with a screw-threaded coupling. Deionized water was injected into one side of the U-shape pipe. The time-varying liquid levels were recorded through a camera (Canon EOS 70D). Videos were captured and analyzed to measure penetration flux and pressure difference in Darcy's law. The hydraulic permeability of the water treatment membrane was calculated using the equation shown in the caption of **Fig. S20**.

Healing of ceramic lattices. Ceramic lattices were designed and printed with different densities. The preceramic structures were dried, pyrolyzed, tested, and healed as in the aforementioned process. Before healing, broken lattices were carefully wrapped with VHB tapes to leave the fracture interface open to contact with the bacteria and precipitation medium. The virgin and healed samples were dried and weighted to calculate the relative density of the lattices in **Fig. 4IJ**.

Autonomous healing of ceramic armor. A set of 3D-architected ceramic armor was fabricated as the aforementioned process. The armor was immersed in bacteria-saturated growth medium over 1 day and transferred into precipitation medium for 4 h. The armor was taken out from liquid before using. A weight-drop (10g) over 5cm was used to damage the armor, and a weight-drop over 15mm was used to create the testing impact force. An accelerometer (Model 352C22) was used to measure the acceleration signal. During the autonomous healing process, moisture was well controlled to prevent the liquid evaporation.

2. Theory of precipitation growth

The bacterial-precipitation enabled interfacial healing includes the following processes: (1) The bacteria-assisted chemical reaction to produce solute $CaCO_3$ following the chemical schemes shown in **Fig. S12** (7-9). (2) Once the solute $CaCO_3$ is oversaturated in the solution, it will precipitate as crystal particles around the surface-attached bacteria. The precipitation particles will grow bigger and coarse. (3) Once the precipitation fully bridges the interface gap, the sample is healed.

Although the microbially-induced mineral precipitation has been modeled in sand systems(7-9), these studies are primarily focused on the precipitation of isolated crystal particles within the solution. It is still elusive how to model the precipitation growth on a surface.

The chemical reactions related to the production of solute $CaCO_3$ are shown in **Fig. S12** (7-9). First, the urea ($CO(NH_2)_2$) activated by the bacteria-produced urease undergoes a ureolysis reaction to produce the ammonia. Ammonia has a reaction with water to form ammonium and hydroxide. The hydroxide dissociates the carbonic acid to form carbonate ions that react with the calcium ions. Effectively, the overall reaction can be considered as the reaction of urea and calcium ions under the activation of the bacteria-produced urease: $CO(NH_2)_2 + 2H_2O + Ca^{2+} \rightarrow 2NH_4^+ +$

$CaCO_3$. We change the precipitation medium and bacterial nutrient every two days to provide a nearly constant concentration of urea, Ca^{2+} and urease. Here we make a bold assumption that the solute $CaCO_3$ concentration C_c immediately produced from the above reaction remains almost the same over the precipitation process.

Physically, the concentration of soluble $CaCO_3$ in the water (denoted as C_s) is very low (0.013 g/L)(10). If the concentration of solute $CaCO_3$ C_c is higher than C_s, the solution is in the oversaturated state. Under an adequate condition, the $CaCO_3$ precipitates as crystals. Bacteria provide excellent nuclei for $CaCO_3$ precipitation(11, 12). The $CaCO_3$ crystal is expected to first nucleate around the bacteria sites and then gradually grow out to fill the fracture gap. Here we consider the precipitation growth around one individual bacterium (**Fig. S14A**).

The precipitation growth can be understood as follows with a schematic in **Fig. S14AB**. The bacterium is located at *r*=0, and the precipitation front is at *r*. Within the area 0-r is in the precipitation state with the molar concentration of $CaCO_3$ within the solid precipitation as C_p. Right at precipitation front r^+, the molar concentration of solute $CaCO_3$ is C_s; while at the location far from the precipitation front, the molar concentration of solute $CaCO_3$ is C_c. The molar concentration profile of $CaCO_3$ around the precipitation front is shown in **Fig. S14B**. If the front moves by a small distance *dr* within a small time *dt*, the number of $CaCO_3$ atoms needed for such a movement is given by $(C_p - C_s)(4\pi r^2)dr$. Since $CaCO_3$ atoms are supplied to the front by diffusion, using the Fick's first law, we can estimate the number of $CaCO_3$ atoms that diffuse in time dt as $D(4\pi r^2)(dC/dx)dt$, where D is the diffusion coefficient of $CaCO_3$ atoms within the solution and C is the concentration of solute $CaCO_3$ in the solution. Equating these two quantities, we obtain the movement velocity as(11-13)

$$\frac{dr}{dt} = \frac{D}{C_p - C_s}\frac{dC}{dr} \tag{S1}$$

To estimate dC/dr, we consider a simplified concentration profile shown in **Fig. S14C**. The concentration gradient can be estimated as

$$\frac{dC}{dr} \approx \frac{C_c - C_s}{L} \tag{S2}$$

where L is the effective length of the concentration tail. Using the mass balance between the two shadow areas in **Fig. S14C**, we obtain

$$\left(\frac{2}{3}\pi r^3\right)\left(C_p - C_c\right) = \frac{2}{3}\pi\left[(L+r)^3 - r^3\right]\left(\frac{C_c - C_s}{2}\right) \tag{S3}$$

We thus can obtain L as

$$L = \left[\left(\frac{2C_p - C_c - C_s}{C_c - C_s}\right)^{1/3} + 1\right]r \tag{S4}$$

Integrating Eqs. S1, S2, and S4, we obtain

$$\frac{dr}{dt} = \frac{D}{C_p - C_s}\frac{C_c - C_s}{\left[\left(\frac{2C_p - C_c - C_s}{C_c - C_s}\right)^{1/3} + 1\right]r} \tag{S5}$$

Solving Eq. S5 leads to the analytic solution for the evolution law for the diameter of the precipitated particle as

$$d = 2r = \sqrt{\frac{8\left(C_c - C_s\right)}{\left[\left(\frac{2C_p - C_c - C_s}{C_c - C_s}\right)^{1/3} + 1\right]\left(C_p - C_s\right)}}\sqrt{Dt} \tag{S6}$$

Therefore, the diameter of the precipitated particle should follow a scaling law $d \propto \sqrt{t}$.

3. Supplementary tables

Table S1. The comparison among three repairing methods of ceramics: bacteria-assisted healing, existing healable bulk ceramics through oxidation or re-sintering, and epoxy glue.

Feature	Bacteria-assisted healing	Existing healable bulk ceramic	Epoxy glue
Healing at room temperature	Yes	No	Yes
Energy cost	Low	High	Low
High strength of healing interface	Yes	Yes	No
Deep crack healing	Yes	Yes	No
Applicable to 3D-printed ceramics	Yes	No	Limited
Corrosion resistance to salt	Yes	Yes	Yes
Corrosion resistance to alkali	Yes	Yes	No
Corrosion resistance to oxidant	Yes	Yes	No
Resistance to wear	Yes	Yes	No
Sustain high temperature	Up to 750ºC	Above 1000 ºC	At best 200-300 ºC

Table S2. Parameters used in cohesive-fracture simulations. Definitions of Young's modulus and tensile strength of the cohesive element are shown in **Fig. S15**. The Young's moduli of the porous ceramic and the cohesive element zone ($CaCO_3$ precipitation) were measured through compressive tests. The Poisson's ratios are estimated based on common Poisson's ratios for stiff solids. The tensile strengths of the cohesive element zone ($CaCO_3$) for various healing days are roughly estimated based on a scaling law $S_{cc} \propto \eta$, where η is the mean covered area ratio shown in **Fig. S10**.

	Physical meaning	**Day 4 healing**	**Day 6 healing**	**Day 8 healing**	**Day 10 healing**
$\boldsymbol{E}$	Young's modulus of ceramic (MPa)	175	175	175	175
$\boldsymbol{\gamma_1}$	Poisson's ratio of ceramic	0.3	0.3	0.3	0.3
$\boldsymbol{E_{cc}}$	Young's modulus of cohesive element (MPa)	45	182	242	290
$\boldsymbol{\gamma_2}$	Poisson's ratio of cohesive element	0.3	0.3	0.3	0.3
$\boldsymbol{S_{cc}}$	Tensile strength of cohesive element (MPa)	0.35	1.21	1.62	1.94

4. Supplementary figures and captions

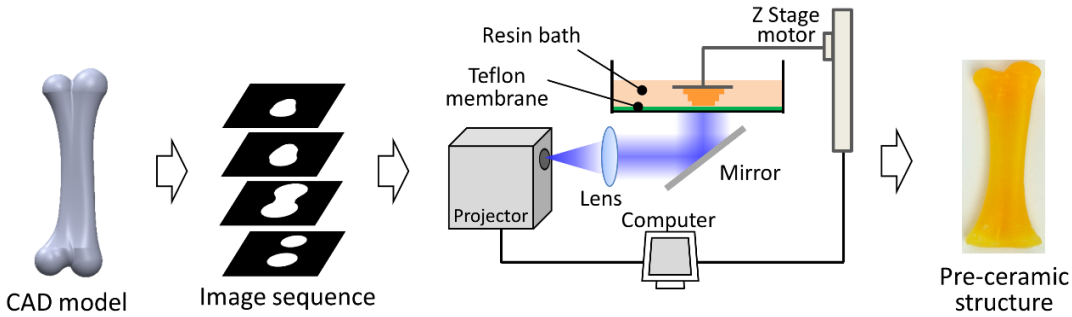

Figure S1. **Additive manufacturing of pre-ceramic polymer structures** (2-4). A CAD model is first sliced into a sequence of images. These 2D slice images, illuminated with UV/blue light from a light-emitting diode, are sequentially projected onto a transparent window. On the window, the liquid photoresin, capped into a prescribed height by a printing stage, is cured by the light and attached to the printing stage. As the printing stage is lifted off, the fresh resin refluxes beneath the printing stage. By lowering down the stage by a prescribed height and illuminating the resin with a subsequent slice image, a new layer can be printed and bonded onto the former layer. To eliminate the adhesion between the solidified resin and bath, an oxygen-permeable membrane (Teflon fluoropolymer, CSHyde, USA) is attached to the bottom, inducing a thin layer (~5-20μm) of the oxygen-rich dead zone to quench the photopolymerization. By repeating these processes, we can print a pre-ceramic polymer structure.

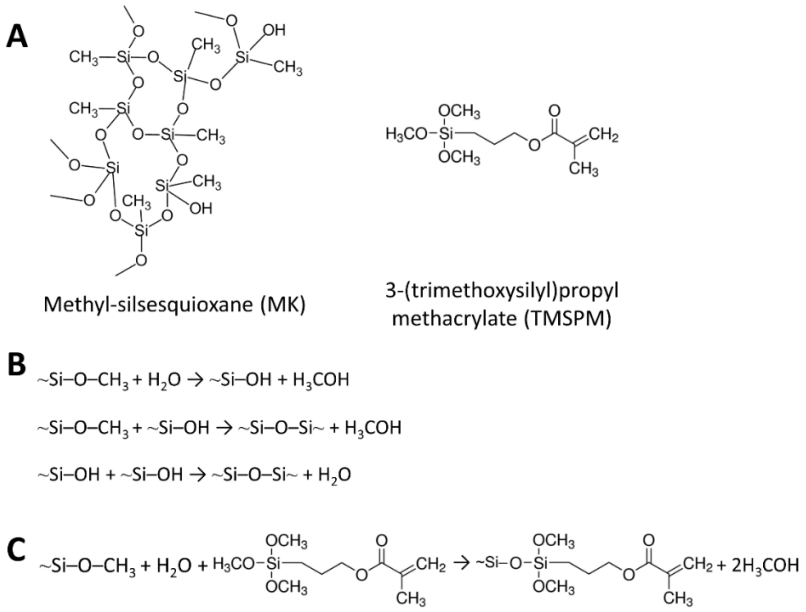

Figure S2. **Materials and synthesis of the pre-ceramic resin**. (A) Chemical structures of methyl-silsesquioxane (MK) and 3-(trimethoxysilyl)propyl methacrylate (TMSPM). (B) The hydrolysis and condensation reactions of alkoxysilyl groups (Si-O-R) (1, 14, 15). (C) The hydrolysis and condensation reaction between MK and TMSPM to attach the acrylate group to the MK network. The acrylate group can enable photo-initiated polymerization.

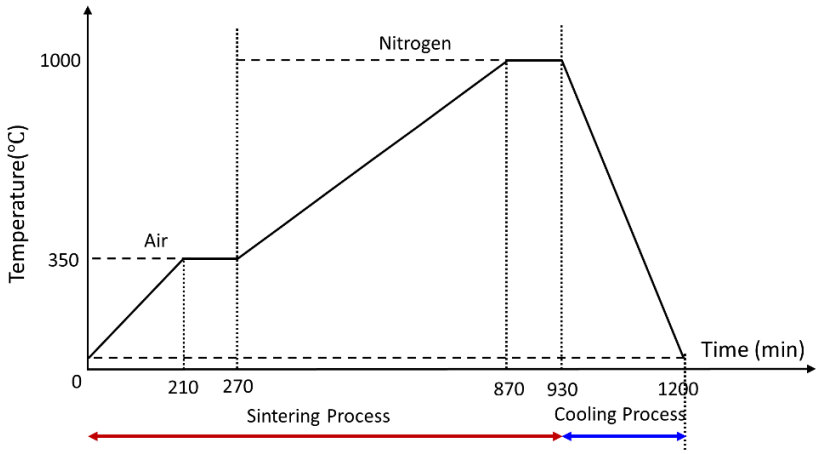

Figure S3. Temperature history of sintering of the pre-ceramic polymer structures into ceramic structures.

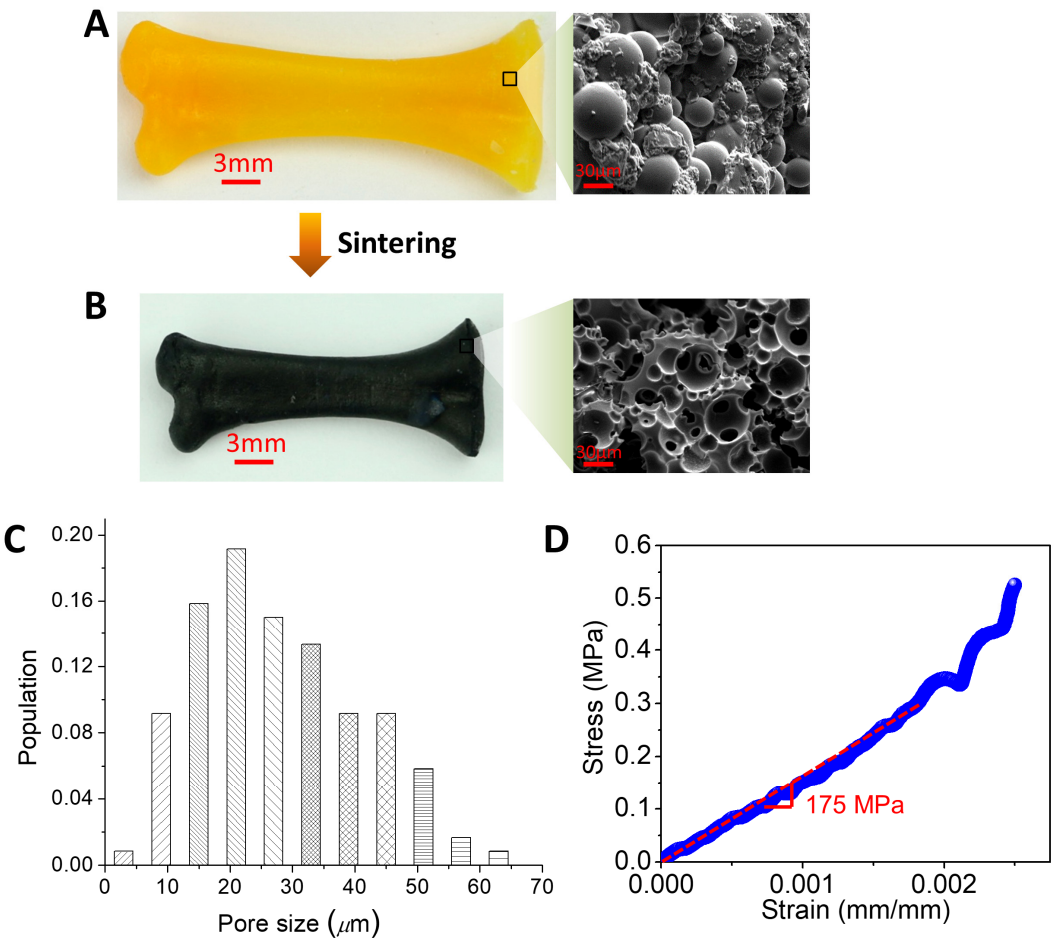

Figure S4. Samples and microstructures of (A) pre-ceramic structure and (B) ceramic structure. (C) Pore size distribution of ceramics with mean PMMA particle size 48 μm. The mean pore size is calculated as 28 μm. (D) The stress-strain curve of the porous ceramic (porosity 56.4%) under a compression test. The Young's modulus is measured as ~175 MPa.

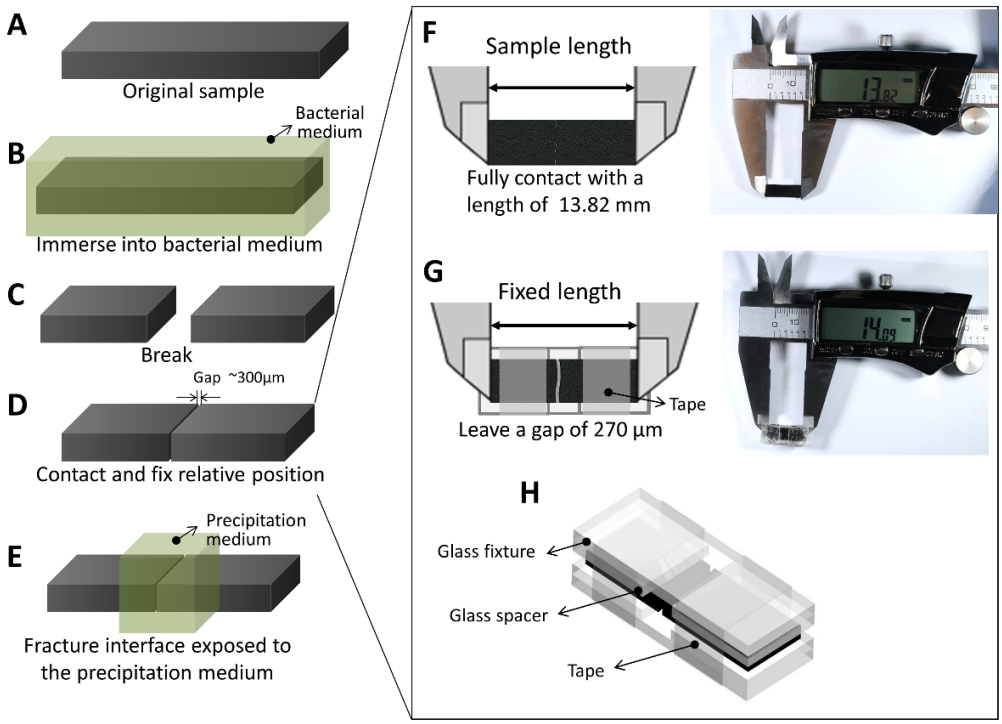

Figure S5. Experimental process of the bacteria-induced interfacial healing of ceramics. The sample was first immersed into a medium containing urease-producing bacteria *Sporosarcina pasteurii* for 24 h to enable the bacteria to attach to pore surfaces (A-B). Then the sample was broken into two parts (C). Two fractured pieces were brought into contact with a very small gap distance (~300 μm) and the relative position was fixed with glass supports and VHB tapes (D). VHB tapes were used to cover the region outside of the fracture interface region. Finally, the fracture interface region was exposed to a precipitation medium (E). On a certain healing day, the sample was taken out to measure the interfacial strength using the three-point bending test. The corresponding healing interface was imaged using a scanning electron microscope (SEM). (F-H) The sample fixture process. A caliper was used to quantify and maintain the gap distance. The sample with a gap distance of ~300 μm was fixed by glass spacers and fixtures with VHB tapes.

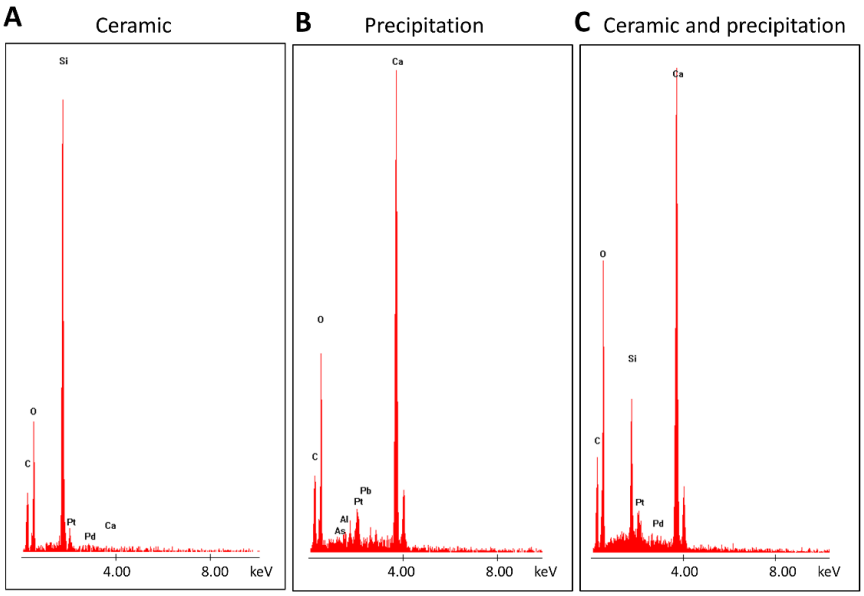

Figure S6. Energy dispersive X-ray microanalyses of (A) ceramics, (B) precipitated crystals, and (C) ceramic and precipitated crystals. The results show that the ceramics (SiOC) primarily consist of C, O, and Si, and that the precipitated crystal primarily consist of C, O, and Ca.

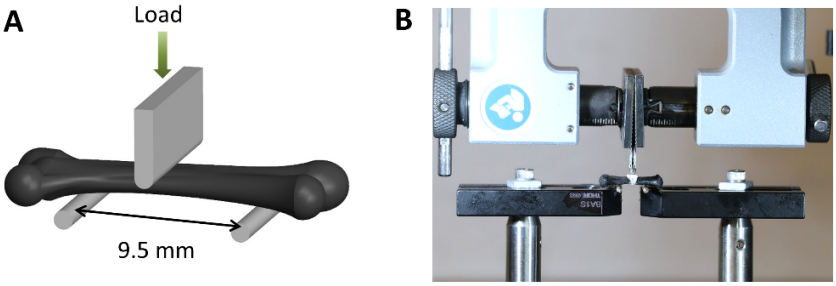

Figure S7. (A) Schematic and (B) experimental setup of the three-point-bending test of a ceramic bone.

Figure S8. Measurement of the flame temperature of a lamp fire that is ignited from a mixture of ethanol (70%) and water (30%) with a Poster digital thermocouple thermometer. The flame temperature is 650-750 °C.

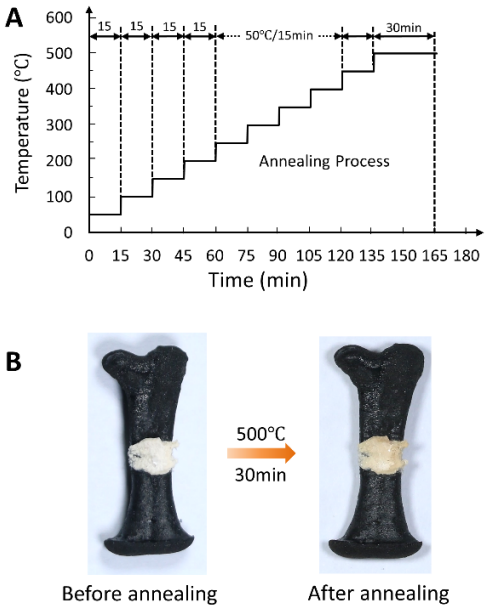

Figure S9. (A) The temperature history of the annealing of a healed ceramic bone. (B) The healed ceramic bone before and after the annealing process. The healing interface does not show any evident change except the color becomes slightly brown.

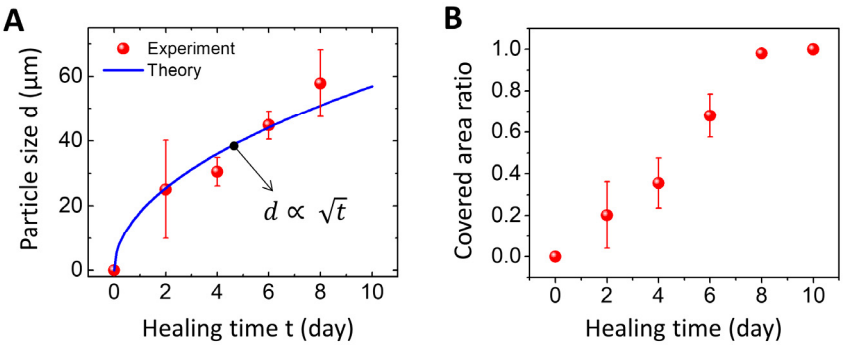

Figure S10. The particle size (A) and the covered area ratio (B) of the precipitated crystals as functions of the healing time. The result of particle size is compared with the theoretically predicted law: $d \propto t^{1/2}$, where d is the particle size and t is the healing time. Error bars represent standard deviations for 3-5 samples.

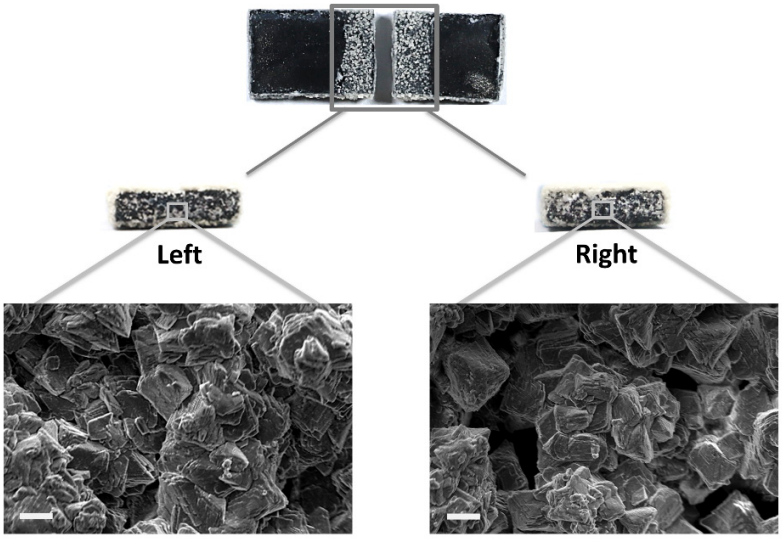

Figure S11. A broken healed sample on day 10 and corresponding SEM images of two fracture interfaces. The scale bars represent 30 μm.

$$CO(NH_2)_2\ (Urea) + 2H_2O \xrightarrow{urease} 2NH_3 + H_2CO_3$$

$$2NH_3 + 2H_2O \leftrightarrow 2NH_4^+ + 2OH^-$$

$$H_2CO_3 + OH^- \rightarrow HCO_3^- + 2H_2O$$

$$HCO_3^- + OH^- + Ca^{2+} \rightarrow CaCO_3$$

$$\Downarrow$$

$$CO(NH_2)_2 + 2H_2O + Ca^{2+} \xrightarrow{urease} 2NH_4^+ + CaCO_3$$

Figure S12. The chemical reactions related to the precipitation of $CaCO_3$(7-9). First, the urea ($CO(NH_2)_2$) activated by the bacteria-produced urease undergoes a ureolysis reaction to produce the ammonia. Ammonia has a reaction with water to form ammonium and hydroxide. The hydroxide dissociates the carbonic acid to form carbonate ions that react with the calcium ions. Effectively, the overall reaction can be considered as the reaction of urea and calcium ions under the activation of the bacteria-produced urease: $CO(NH_2)_2 + 2H_2O + Ca^{2+} \rightarrow 2NH_4^+ + CaCO_3$.

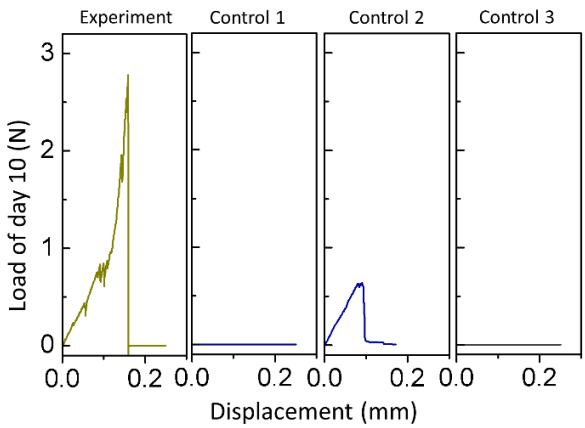

Figure S13. The load-displacement curves of the experiment case and three control cases in 3PB tests for 10-day healing. The samples of control 1 and control 3 are not healed.

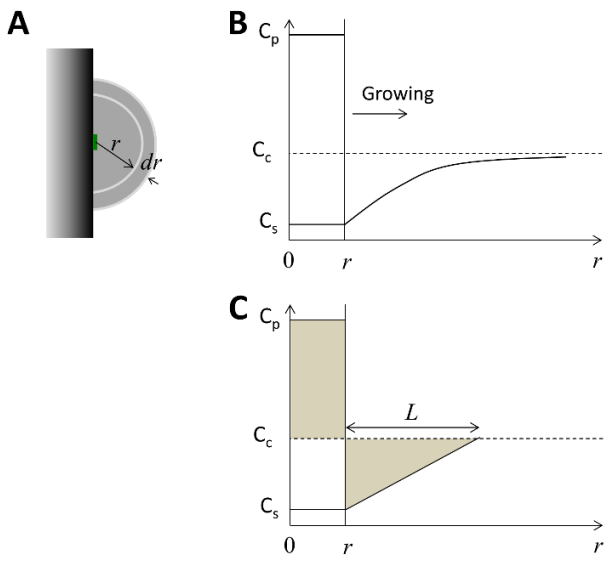

Figure S14. (A) A schematic to show a half-spherical crystal around a bacterium (green bead). (B) The diffusion-controlled growth of a precipitated crystal particle. C_p is the concentration of the solute in the precipitate. C_c is the concentration of the solute in the solution. C_s is the concentration of the solution after precipitation. (C) Simplification of the concentration profile.

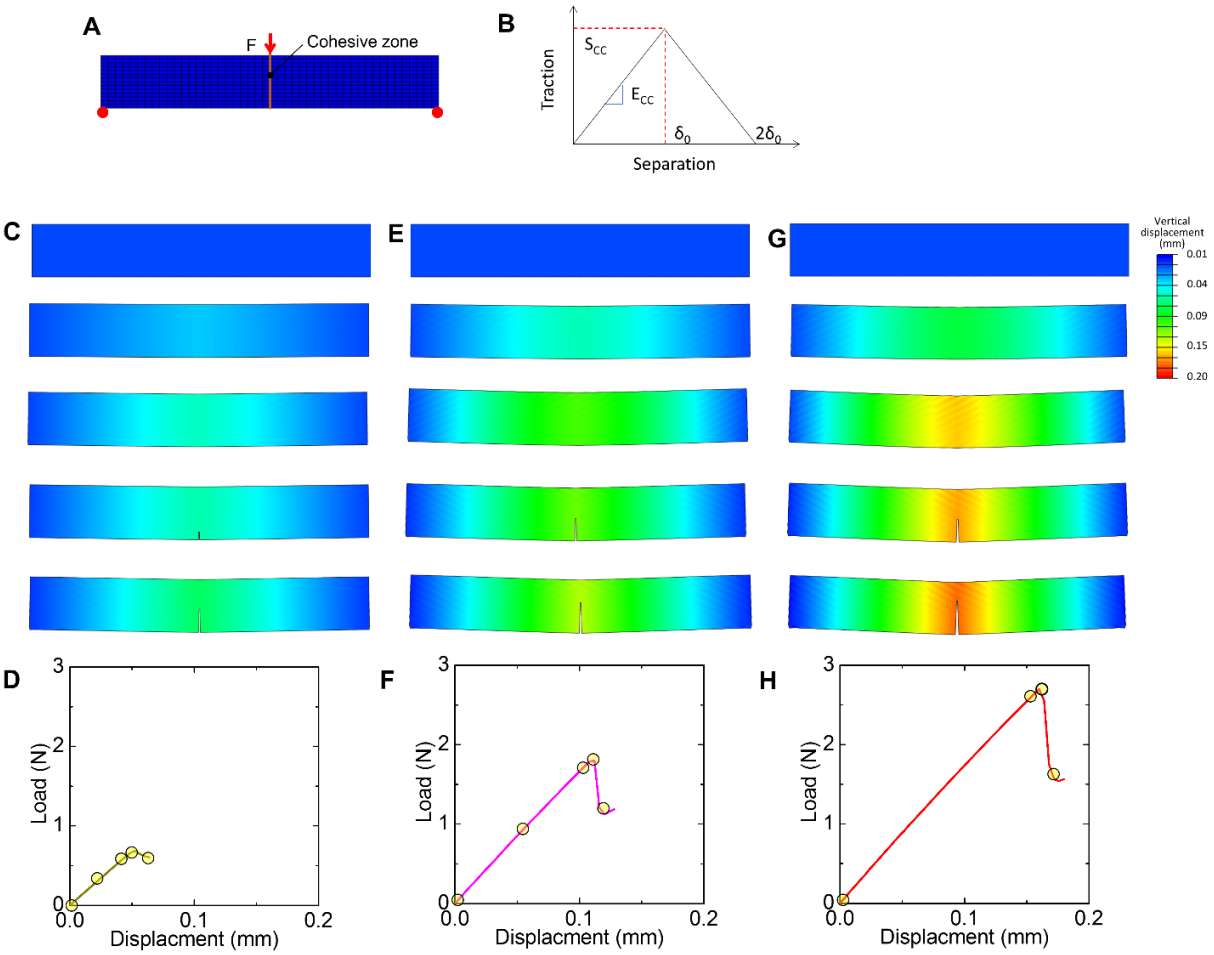

Figure S15. (A) Setup for cohesive-fracture simulations. CPS4R elements are employed to model the ceramic part and COH2D4 elements for the cohesive zone. (B) Bilinear Traction-displacement relationship of the cohesive zone element. The parameters used in simulations are presented in Table S2. E_{cc} is Young's modulus of the cohesive element and S_{cc} is the tensile strength of the cohesive element. The simulation sequences (C, E, and G) and load-displacement relationships (D, F, and H) for weak healed interface (day 4 healing, C-D), moderate healed interface (day 6 healing, E-F), and strong healed interface (day 10 healing, G-H). The dots in D, F and H represent the states of the simulations shown in C, E, and G, respectively.

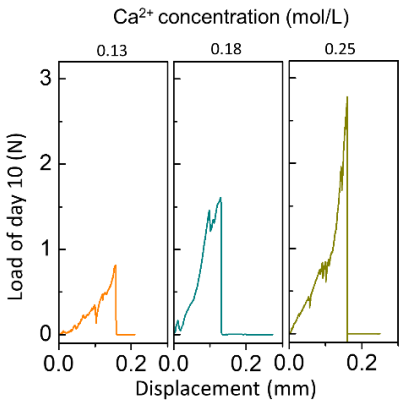

Figure S16. The load-displacement curves of healed ceramic plates with various Ca^{2+} concentrations in 3PB tests for 10-day healing.

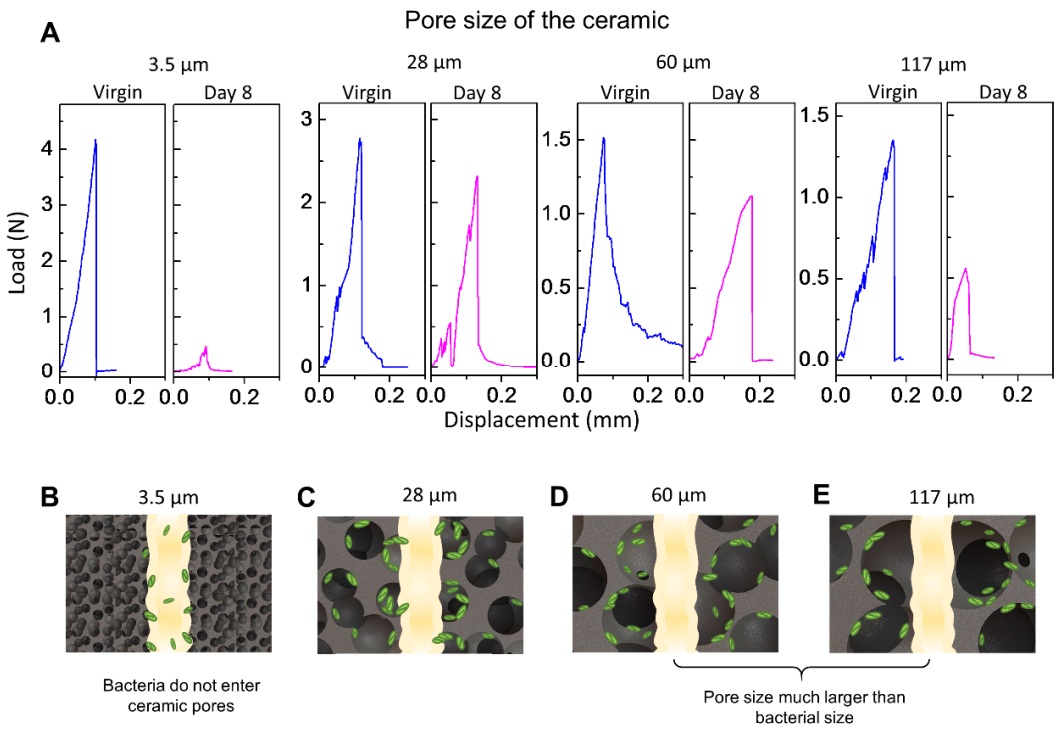

Figure S17. (A) The load-displacement curves of virgin and healed ceramic plates for various pore sizes in 3PB tests for 8-day healing. (B-E) Schematics to show fracture interfaces of bacteria-loaded porous ceramics with various mean pore sizes: (B) 3.5 μm, (C) 28 μm, (D) 60 μm, and (E) 117 μm.

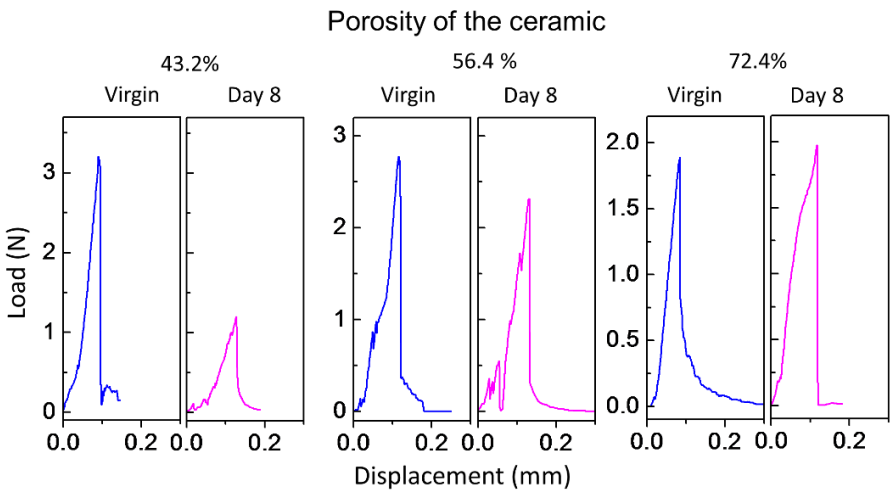

Figure S18. The load-displacement curves of virgin and healed ceramic plates for various porosity in 3PB tests for 8-day healing.

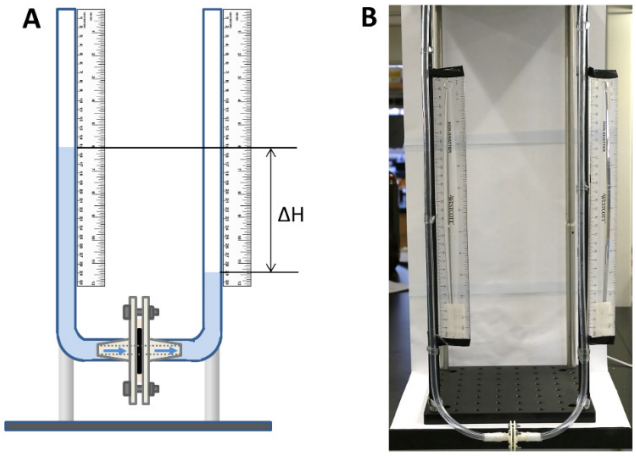

Figure S19. (A) Schematic and (B) experimental setup for testing the hydraulic permeability of the ceramic water treatment membranes. The permeability of the membrane is calculated by using $Q = \kappa\left(\frac{S}{h\mu}\right)\Delta p$, where Q is the flow volume rate (m^3/s), κ is the permeability (m^2), S is the cross-section area of the flow pathway, h is the thickness of the membrane, μ is the viscosity of the water (Pa·s), the pressure drop $\Delta p = \rho g \Delta H$, ρ is the density of the water, g is the gravity constant, and ΔH is the water height difference shown in (A). We plot the relationship between Q and Δp in **Fig. 4F** and fit the slope as $\kappa S/(h\mu)$.

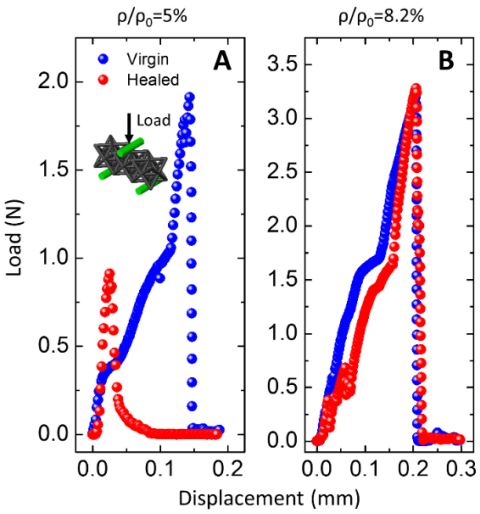

Figure 20. The load-displacement curves of the virgin and healed Octet ceramic lattices with different relative densities: (A) ρ/ρ_0=5% and (B) ρ/ρ_0=8.2%, where ρ and ρ_0 are densities of the ceramic lattices and the solid ceramic, respectively.

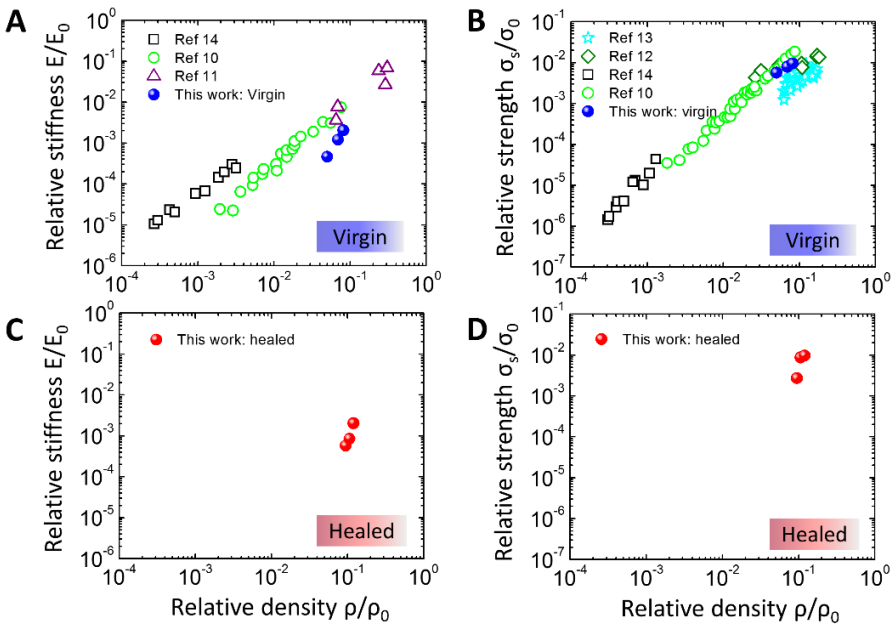

Figure 21. The relative stiffnesses E/E_0 (AC) and the relative strengths σ_s/σ_0 (BD) of the virgin ceramic lattices (AB) and healed ceramic lattices (CD) as functions of relative densities ρ/ρ_0. The results of existing studies on ceramic lattices are plotted in (A) and (B) (16-20). Note that all the existing results on the relative strengths are relative compressive strengths, while the current results shown in (BD) are relative tensile strengths.

5. Supplementary movie captions

Movie S1: A movie to show that the healed interface can safely sustain the rinsing of a strong alkali solution (NaOH, 4.8 mol/L) and a strong oxidant solution (H_2O_2, 8.8 mol/L).

Movie S2: A movie to show that the healed interface can sustain a fire burning (650-750 °C) without breaking the healed interface for over 10 min. The fire burning used to test the healed sample was ignited from a mixture of ethanol (70%) and water (30%).

Movie S3: A movie to show the simulated cohesive fracture process of the healed sample with a weak interface for day 4 healing. The used parameters for the finite element simulation are listed in Table S2.

Movie S4: A movie to show the simulated cohesive fracture process of the healed sample with a moderate interface for day 6 healing. The used parameters for the finite element simulation are listed in Table S2.

Movie S5: A movie to show the simulated cohesive fracture process of the healed sample with a strong interface for day 10 healing. The used parameters for the finite element simulation are listed in Table S2.

Reference

1. Zanchetta E*, et al.* (2016) Stereolithography of SiOC ceramic microcomponents. *Adv. Mater.* 28(2):370-376.
2. Wang Q*, et al.* (2016) Lightweight Mechanical Metamaterials with Tunable Negative Thermal Expansion. *Phys. Rev. Lett.* 117(17):175901.
3. Jiang Y & Wang Q (2016) Highly-stretchable 3D-architected mechanical metamaterials. *Sci Rep.* 6:34147.
4. Yu K, Xin A, Du H, Li Y, & Wang Q (2019) Additive manufacturing of self-healing elastomers. *NPG Asia Mater.* 11(1):7.
5. Stocks-Fischer S, Galinat JK, & Bang SS (1999) Microbiological precipitation of CaCO3. *Soil Biology and Biochemistry* 31(11):1563-1571.
6. Bang SS, Galinat JK, & Ramakrishnan V (2001) Calcite precipitation induced by polyurethane-immobilized Bacillus pasteurii. *Enzyme and microbial technology* 28(4-5):404-409.
7. Hommel J*, et al.* (2015) A revised model for microbially induced calcite precipitation: Improvements and new insights based on recent experiments. *Water Resources Research* 51(5):3695-3715.
8. Ebigbo A*, et al.* (2012) Darcy‐scale modeling of microbially induced carbonate mineral precipitation in sand columns. *Water Resources Research* 48(7).
9. Barry ZT (2018) Mathematical and Computational Considerations of a Model of Microbiologically Induced Calcite Precipitation.
10. Tegethoff FW, Rohleder J, & Kroker E (2001) *Calcium carbonate: from the Cretaceous period into the 21st century* (Springer Science & Business Media).
11. Porter DA, Easterling KE, & Sherif M (2009) *Phase Transformations in Metals and Alloys, (Revised Reprint)* (CRC press).
12. Balluffi RW, Allen S, & Carter WC (2005) *Kinetics of materials* (John Wiley & Sons).
13. Zener C (1949) Theory of growth of spherical precipitates from solid solution. *Journal of applied physics* 20(10):950-953.
14. Chae HS, Song SJ, & Park YH (2008) Preparation of Spherical Poly (methylsilsesquioxanes) Beads and Their Properties. *Molecular Crystals and Liquid Crystals* 492(1):28/[392]-338/[402].
15. Padovani AM, Riester L, Rhodes L, Allen SAB, & Kohl PA (2002) Chemically bonded porogens in methylsilsesquioxane II. Electrical, optical, and mechanical properties. *Journal of The Electrochemical Society* 149(12):F171-F180.
16. Meza LR, Das S, & Greer JR (2014) Strong, lightweight, and recoverable three-dimensional ceramic nanolattices. *Science* 345(6202):1322-1326.
17. Muth JT, Dixon PG, Woish L, Gibson LJ, & Lewis JA (2017) Architected cellular ceramics with tailored stiffness via direct foam writing. *Proceedings of the National Academy of Sciences* 114(8):1832-1837.
18. Eckel ZC*, et al.* (2016) Additive manufacturing of polymer-derived ceramics. *Science* 351(6268):58-62.
19. Minas C, Carnelli D, Tervoort E, & Studart AR (2016) 3D Printing of Emulsions and Foams into Hierarchical Porous Ceramics. *Adv. Mater.* 28(45):9993-9999.
20. Zheng X*, et al.* (2014) Ultralight, ultrastiff mechanical metamaterials. *Science* 344(6190):1373-1377.